PCCP

Accepted Manuscript

This is an *Accepted Manuscript*, which has been through the Royal Society of Chemistry peer review process and has been accepted for publication.

Accepted Manuscripts are published online shortly after acceptance, before technical editing, formatting and proof reading. Using this free service, authors can make their results available to the community, in citable form, before we publish the edited article. We will replace this *Accepted Manuscript* with the edited and formatted *Advance Article* as soon as it is available.

You can find more information about *Accepted Manuscripts* in the Information for Authors.

Please note that technical editing may introduce minor changes to the text and/or graphics, which may alter content. The journal's standard Terms & Conditions and the Ethical guidelines still apply. In no event shall the Royal Society of Chemistry be held responsible for any errors or omissions in this *Accepted Manuscript* or any consequences arising from the use of any information it contains.

Phase stability of Li-Mn-O oxides as cathode materials for Li-ion Batteries: insights from *ab initio* calculations

R. C. Longo,[a] F. T. Kong,[a] Santosh KC,[a] M. S. Park,[b] J. Yoon,[b] D. -H. Yeon,[b] J. -H. Park,[b] S. -G. Doo,[*b] and K. Cho[*a]

In this work, we present a density-functional theory (DFT) investigation of the phase stability, electrochemical stability and phase transformation mechanisms of the layered and over lithiated Mn oxides. This study includes the thermodynamic stability of Li and oxygen vacancies, to examine the electrochemical activation mechanisms of these cathode materials. DFT calculations provide phase diagrams of Li-Mn-O system in both physical and chemical potential spaces, including the crystals containing vacancies as independent phases. The results show ranges of electrochemical activity for both layered $LiMnO_2$ and over lithiated Li_2MnO_3. By using a thermodynamic model analysis, we found that the required temperature for oxygen evolution and Li vacancy formation is too high to be compatible with any practical synthesis temperature. Using solid-state transition calculations, we have identified key steps in the phase transition mechanism of the layered $LiMnO_2$ into the spinel phase. The calculated effects of pH on the Li-Mn-O phase stability have elucidated the Mn^{2+} formation mechanism from spinel phase under acid condition.

1 Introduction

The wide usage of rechargeable Li-ion batteries in portable electronic devices and electric vehicles requires high energy density, fast charge/discharge rate and long cycling lifetimes.[1–5] Cathode materials play the most important role in determining the performance of the battery, because they constitute the major bottleneck to improve it. Currently, layered $LiCoO_2$ oxides are the most common cathode material in the market.[6–11] Typically, the maximum theoretical capacity of $LiCoO_2$ is about 274 mAh/g,[12] and practical capacity remains larger than 130 mAh/g after more than forty cycles of charge and discharge.[13] However, $LiCoO_2$ has many important drawbacks, including a non-negligible instability at the end of the charging process and decomposition at high temperatures.[14–18] Moreover, the Co is becoming more expensive due to its relatively low abundance in the earth's crust. To overcome these difficulties, both $LiNiO_2$ and $LiMnO_2$ have been widely explored as an alternative to the Co oxides.[19–26] Both of them suffer from their own disadvantages for practical purposes. For example, the main problem of $LiMnO_2$ is a structural transformation to the spinel phase during elec-

trochemical cycling, which hinders subsequent Li insertion and/or removal.[27,28]

One of the most promising alternatives from a practical point of view is the Over-Lithiated-Oxide (OLO) cathode material Li_2MnO_3 and its composite with $Li(Ni,Co,Mn)O_2$.[29] After losing most of the Li ions during the charging process, the OLO gradually undergoes a phase transition into the layered oxide $LiMnO_2$.[29–31] Consequently, the cathode material used in practical applications is a composite structure, *i.e.*, a compound of the form $xLi_2MnO_3(1-x)LiMnO_2$, where the ideal x ratio is something to be determined experimentally.[29–36] The OLO phase of the composite material has the same layered structure as the $LiMnO_2$, but wih a "mixed" Li-Mn layer, instead of pure Mn and Li layer stacking. The additional amount of Li from the OLO phase increases the capacity and the energy density, provided that the stability issues of the layered Mn oxide are solved.[27,28]

There has been numerous experimental studies on the electrochemical performance of the OLO composite Mn layered oxides.[29–33] The problems arise because, despite its high capacity, Li_2MnO_3 presents several hurdles to practical applications: Mn ions are in Mn^{4+} oxidation state in Li_2MnO_3, even when Li ions are not extracted from the crystal (contrary to the Co^{3+} in $LiCoO_2$). Thus, it is difficult to extract Li ions from the stoichiometric Li_2MnO_3 at the usual operating voltage of Li ion batteries (4.1 V *vs.* Li/Li$^+$).[37] Therefore, as Mn^{4+} has been considered as inert in electrochemical reactions, it requires an specific mechanism for activating the material to use it as a cathode. The most common activation process consists

---

Physical Chemistry Chemical Physics Accepted Manuscript

of the injection of oxygen vacancies by elevating the potential to 4.5 V or even higher.[38–40] However, Li_2MnO_3 treated by such activation procedure still needs improvement especially in cyclability for practical purposes.[37] Pasero *et al.* reported the oxygen deficiency in Li_2MnO_3, leading to the formation of Mn^{3+}, but the low amount of oxygen vacancies was not enough to explain the large rechargeable capacity.[41] Lu and Dahn suggested that both Li and O atoms were removed during the first charging, but in a compound with Ni impurities, which can act as electrochemically active species (oxidation of Ni^{2+} to Ni^{4+}).[29] Kim *et al.* suggested that the removal of Li atoms was subsequently accompanied by oxygen loss due to the removal of electrons from the O $2p$ band.[42] Finally, another mechanism, proposed by Robertson and Bruce, is that the charging occurred by the oxidation of the nonaqueous electrolyte and that those generated protons were exchanged for Li ions in Li_2MnO_3.[36]

Parallel to the experimental studies, *ab initio* calculations based on density functional theory (DFT) are a powerful tool to unveil, at the atomic scale, the mechanisms underlying the electrochemical properties of these layered oxides cathode materials.[43–46] Most of the theoretical efforts have been focused on the $LiCoO_2$, from the fundamental and electronic properties,[47–50] to the phase diagrams or Li diffusion behavior.[48,50–54] Although less frequent, there are also several studies devoted to the understanding of the properties of both $LiMnO_2$ and OLO composite materials Li_2MnO_3. For instance, Wang *et al.* studied the thermal stability of the layered oxides,[55] Shin *et al.* reported the solubility of the Mn cations from $xLi_2MnO_3(1-x)LiMO_2$ (M = Mn, Ni, Co) into the surface-treated layer, to prove that the small solubility might account for the improved electrochemical cycling stability and rate capability observed in their own experiments.[56] On the other hand, Okamoto showed that the introduction of O-vacancies activates the Mn sites as the redox center for the Li extraction from Li_2MnO_3.[37] Koyama *et al.* identified a disordered stacking sequence of Mn-Li layers in Li_2MnO_3 to account for the wide potential plateau following the first Li extraction at high potential (4.6 V).[57]

However, as we stated previously, at these high potentials Li extraction is accompanied either by oxygen loss at the surface of the highly delithiated $Li_{1-x}MnO_2$ (0.5<x<1) component with a concomitant reduction of the Mn ions or by the removal of Li and O from the Li_2MnO_3 phase without any change to the tetravalent oxidation state of the Mn cations (*i.e.*, with a net loss of Li_2O).[56] The other important drawback of the layered Mn oxides, the phase transformation into a spinel structure with the removal of Li ions, still remains unsolved.[27,28]

In this work, we have used *ab initio* calculations based on DFT to perform a detailed analysis of the phase composition and thermodynamic stability of $xLi_2MnO_3(1-x)LiMnO_2$. We obtained the phase diagram as a function of temperature to examine the effects of synthesis temperature and oxygen partial pressure on the formation of the different phases and the evolution of their relative stabilities with temperature. Our main goal is to investigate the thermal stability of the Li and/or O vacancies as activation mechanisms of the electrochemical redox activity of the OLO composite structures. Finally, by using a recently developed method to determine solid-state transformations,[58] we will examine the mechanisms that lead to the transformation of the layered Mn oxide into the spinel phase, in an attempt to improve the cycling stability and rate capability of the Mn layered oxides as cathode materials for Li-ion batteries.

2 Methods

2.1 *Ab initio* calculations

All the calculations performed in this work have been done using DFT method as implemented in the Viena *Ab initio* Simulation Package (VASP) code[59,60] within the Projector-Augmented-Wave (PAW) approach.[61] Given the different techniques and problems addressed in this study, we now describe in detail the different theoretical approaches used in our calculations.

2.2 Phase stability

The phase stability of the different compounds studied in our work was obtained by constructing the appropriate Li-Mn-O computational phase diagram. We considered in our calculations all the known binary and ternary compounds with Li, Mn and O, as included in the Inorganic Crystal Structure Database (see Table 1).[62]

The Gibbs free energies of all the compounds need to be compared to construct a phase diagram, because the diagram shows the most stable phases under certain conditions. For the different phases of the Li-Mn-O system, the stability of each phase (with and without defects) is determined by comparing the normalized Gibbs free energies:

$$G(Li_xMn_yO_z) = \frac{G(T,P,Li_xMn_yO_z)}{x+y+z} \qquad (1)$$

As the changes in pressure, volume and entropy have a negligible effect on solids (not for the oxygen molecule, as we will discuss in the next paragraph),[55,63,64] this equation can be approximated as:

$$G(Li_xMn_yO_z) = \frac{G(T,P,Li_xMn_yO_z)}{x+y+z} \approx \frac{E^0(0K,Li_xMn_yO_z)}{x+y+z} \qquad (2)$$

There are only two independent variables in the composition space and, for each phase, the position on a ternary diagram and the normalized Gibbs free energy represent a unique point in 3-D space. The ternary phase diagram is then obtained by taking the convex hull (smallest convex set containing all the Gibbs free energies) and projecting it onto a plane. [63,65]

In a similar way, we can construct the ternary phase diagram using the pH as independent variable. Indeed, assuming that the surface of the cathode material is in equilibrium with bulk water with a specific pH value, [66,67] the oxygen chemical potential of the ternary Li-Mn-O system:

$$\mu(Li-Mn-O) = \mu(Li) + \mu(Mn) + \mu(O) \qquad (3)$$

is related to the water chemical potential:

$$\mu(H_2O) = 2\mu(H) + \mu(O) \qquad (4)$$

The chemical potential of hydrogen is related to the chemical potentials of electrons and protons:

$$\mu(H) = \mu(H^+) + \mu(e^-), \qquad (5)$$

which in turn is related to the pH value by the following relation:

$$\mu(H^+) = \mu_o - pH \times 0.05918 \; eV, \qquad (6)$$

where μ_o is the proton solvation enthalpy in water, [66,67] and the chemical potential of the electrons is assumed to be fixed at the Fermi level of a system of reference. In our work, we chose the OLO Li_2MnO_3 as a reference. Additional tests performed shown that there are no practical changes in the obtained results if we substitute the OLO by any other Li-Mn-O cathode material studied in this work. Using the above equations, we can express the oxygen chemical potential as a function of the pH and, thus, to study the ternary phase diagram as a function of the acidic or basic characteristics of the media.

The total energy calculations were performed using the Perdew-Burke-Ernzerhof (PBE) generalized-gradient approximation (GGA) functional, [68] and the plane-wave cut off used was of 500 eV in all cases. For all the compounds, a k-point mesh within the Monkhorst-Pack scheme [69] was used to ensure a convergence of 1 meV/unit cell. Structural relaxations were performed without including any constraint to a tolerance of 10^{-4} eV in the total energy and 0.01 eV/ Å in the forces on every atom. The initial structures for each compound were taken from the materials project database. [70] All calculations were spin-polarized and both ferromagnetic (FM) and antiferromagnetic (AFM) magnetic configurations were considered. The total energies used to construct the phase diagram correspond to the lower energy magnetic configuration found for each compound.

Although PAW potentials have been extensively used in the study of positive electrode materials for Li-ion batteries, GGA is known to show large errors in the calculation of the electrochemical properties of these materials. The reasons are the different chemical environments during the redox processes: from metallic Li to a transition metal (TM) in a oxyanion group; and also the well-known tendency of the GGA to overestimate the delocalization of the d-redox electrons of the TM and their hybridization with the O p states, which to a large extent determines the electrochemical properties of the cathode material. [71,72] By explicitly including an onsite coulomb, U, and exchange, J, terms in the Hamiltonian (GGA+U approach), we can partially correct the electron over-delocalization (and the self-interaction errors) and accurately calculate the electrochemical properties. [73] It is then crucial to precisely determine the value of the U parameter to perform GGA+U DFT calculations. Although different values have been reported for the U parameter, and they might depend on the crystal structure and the oxidation state of the Mn cation involved, we need to set up a common value throughout all the calculations in order to avoid the strong dependence of the total energy on the U parameter when comparing the formation energies of the different compounds and building the phase diagram. The U parameter has been obtained by means of a linear response method, [72,73] and it was set to 5.2 eV for all the compounds considered in this work. The J value was set to 0 eV in all cases, as only the U-J difference is relevant for the calculations.

To analyze the thermochemistry of an oxide system, it is also important to accurately determine the energy changes occurring during the oxidation reaction. As stated previously, the U parameter accounts for the over-delocalization of the d-electrons of the Mn, but another source of errors comes from the overestimation of the oxygen dimer binding energy and a possible contribution associated with the addition of two electrons to the oxygen p-orbitals to form O^{2-} from O_2. [64,73,74] Thus, by properly determining the chemical potentials of O_2, we can compensate DFT errors and improve the accuracy of the obtained phase diagrams. A correction term for the oxygen molecule is then included in the calculation of the formation energies (the room-temperature enthalpy of O_2 was determined to be -8.95 eV/formula unit). [64,73,74] This term has been obtained by calculating the formation enthalpies of several oxides and comparing them with the experimental values, in order to obtain the best agreement possible for the enthalpy of the oxygen gas molecule. [64] To calculate the phase diagrams at different temperatures, we obtained the dependence of the chemical potential of O_2 with temperature and pressure using the data in the JANAF thermochemical tables. [75]

2.3 Electrochemical stability

To assess the electrochemical stability of a Li-Mn-O system under real experimental conditions, *i.e.*, open to Li or O environments, we build the Li-Mn-O phase diagram in the chemi-

cal potential space. To find meaningful limits for the chemical potentials, we follow the methodology proposed in Ref. [74]. The chemical potentials are not independent, they have to be summed as the free energy of the bulk compound for a stoichiometric system:

$$g_b = \sum x_i \mu_i \tag{7}$$

where x_i is the number of atoms per formula unit of species i. Assuming that the entropic and volumetric contributions are negligible,[55,63,64] the free energy can be approximated by the energy obtained directly from DFT calculations (ε_b). Upper limits for the chemical potentials are established by the pure elements, which are then defined as reference chemical potentials: $\mu_i^* = E_i^0$, where E_i^0 is the energy per atom of the pure element. Metallic Li and O_2 gas phase are the reference states. Lower limits can be defined from the relation between the chemical potentials and the DFT energy of the corresponding bulk compound (equation 3). The valid range of the chemical potential would then be given by: $\varepsilon_f/x_i < (\mu_i - \mu_i^*) < 0$, with the formation energy ε_f defined as: $\varepsilon_f = \varepsilon_b - \sum x_i \mu_i^*$. This equation reflects the stability of every compound with respect to the reference states (in our calculations, we used the fcc phase of Mn as a reference state for the TM). There are similar conditions for the equilibrium of the different compounds on a ternary system. By combining all of them, the phase diagram in the chemical potential space can then be plotted.

2.4 Solid state transformations

The climbing image-nudged elastic band method (CI-NEB) allows us to obtain the minimum energy path (MEP) between a set of two different states.[76–78] Usually, the initial and final states correspond to different configurations of the same system. The challenge of finding reaction paths for solid-solid transformations comes from taking into account that there are two different types of variables, *i.e.*, those describing atomic motion and those describing the geometry of the periodic cell. In the standard CI-NEB method,[77,78] the atomic coordinates are moved according to the forces on the atoms. The analogy for the cell vectors is the stress acting on the material. A relationship between stress, strain and the change in cell vectors is then needed. The last step consists in coupling cell and atomic variables (they have different units and scaling relations) and combining them in a single vector. The method is described in detail in Ref. [58]. In our calculations, the initial state is a layered Mn oxide with half of the Li atoms removed (to match the stoichiometry of the spinel structure), and the final state is the spinel phase.

3 Results

3.1 Li-Mn-O phase diagram in the chemical potential space

We have obtained the formation energies of a series of Li-Mn-O compounds, taking into account the correction for the binding energy of the O_2 molecule aforementioned. The results are shown in Table 1 (for each stoichiometry, only the most stable compound is shown). All of them correspond to a U value of 5.2 eV. Although the total energy is obviously affected by the specific value of the U parameter, the general trends in the formation energies are invariant to small deviations from the adopted value.

Table 1 Calculated formation energies of stable bulk compounds in the Li-Mn-O system. For each stoichiometry, only the most stable compound is shown.

Compound	Structure	Space group	ε_f (eV/atom)
Mn	fcc	$Fm\bar{3}m$	-6.0269
Li	bcc	$Im\bar{3}m$	-1.8948
$\frac{1}{2}O_2$	gas phase		-4.9295
$LiMnO_2$	Layered O3	$R\bar{3}m$	-1.9960
Li_2MnO_3	Layered O3	$C2/m$	-1.9293
$LiMn_2O_4$	Spinel	$Fd\bar{3}m$	-1.8389
$Li_2Mn_3O_7$	Triclinic	$P\bar{1}$	-1.7306
MnO	Rocksalt	$Fm\bar{3}m$	-2.1853
Mn_2O_3	α	$Pbca$	-1.9137
Mn_3O_4	Hausmannite	$I4_1/amd$	-2.0491
Mn_2O_5	Mullite	$P4/mbm$	-0.8240
Mn_5O_8	Monoclinic	$C2/m$	-1.8028
MnO_2	Trigonal	$R\bar{3}m$	-1.5107
Li_2O	Fluorite	$Fm\bar{3}m$	-1.8646
Li_2O_2	Hexagonal	$P6_3/mmc$	-1.4381

The resulting phase diagram in the chemical potential space is shown in Fig. 1. The picture shows the correlations between the different phases within the system, as a function of both the chemical potential of Li, $\mu(Li)$, and oxygen, $\mu(O)$. As we have chosen metallic Li as the reference state ($\mu^*(Li)$), the Li chemical potential represents the negative of the voltage against Li|Li$^+$ extraction/insertion.[74] On the other hand, the chemical potential of the O_2 molecule at 0 K sets the reference state for the oxygen (with the correction aforesaid, dashed line in the figure). The chemical potential of the oxygen gas phase strongly depends on the pressure and temperature. The dotted line indicates the chemical potential $\mu(O)$ at room temperature and ambient pressure, conditions under which most of the synthesis experiments are carried out. The difference is less than 0.2 eV with respect to the O_2 reference state. In our study, we used the Mn fcc bulk as reference state for the TM, due to the wide range of experimental values existent for the Mn oxides. The equilibrium between two different phases is marked with

a line, and the points where two lines intersect show the region where three different phases coexist. The compounds with a stability window above the oxygen chemical potential reference state ($\mu^*(O)$) are thermodynamically not stable at 0 K. The Li oxides are also represented with lines because they are independent on the Mn chemical potential (this fact restricts the number of independent chemical potentials to one) and the Mn oxides are represented by areas, because $\mu(O)$ is independent of $\mu(Li)$ for these compounds.
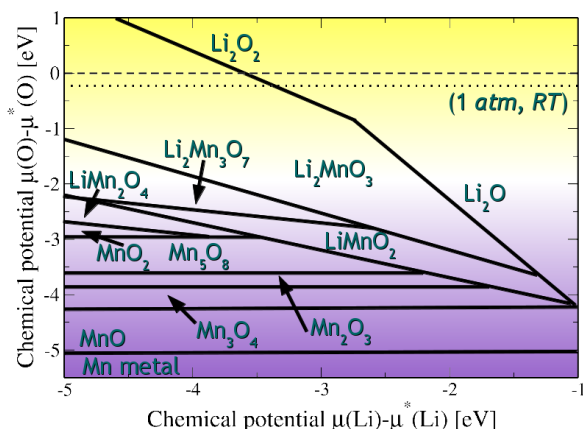
Fig. 1 Phase diagram of the Li-Mn-O system in the chemical potential space. The color shading shows the acidic (yellow) and basic (violet) environments, respectively.

The phase diagram shows that there are no partially delithiated phases (Li_xMnO_2) present, a fact that supports the well-known experimental evolution into the spinel structure.[27,28] This phase (spinel) shows a stability window beyond 3.5 V *vs.* Li|Li$^+$ extraction/insertion. The triclinic $Li_2Mn_3O_7$ also appears as a stable phase under certain chemical potential conditions, as we will discussed in the last section. In an oxidizing atmosphere, the OLO phase appears to be the most thermodynamically stable but, upon reduction (*i.e.*, oxygen evolution), it transforms into the standard layered oxide, $LiMnO_2$. While the overlithiation leads to the formation of Li_2O (under reduction) and Li_2O_2 (under oxidizing conditions), the delithiation (under enough reducing conditions) leads to the formation of the different Mn oxides. Both Li_2O and Li_2O_2 are the main reaction products of the activation mechanisms (Li and/or O vacancies) of the redox activity of the OLO composite structure.[38–40] The lowest region corresponds to the Mn fcc bulk, which is taken as the reference state in the calculation of the formation energies.

3.2 Phase stability of Li vacancy and O evolution activation mechanisms

We have calculated the formation energies of O and Li vacancies in both $LiMnO_2$ and Li_2MnO_3 crystals, in order to verify if the temperatures of formation and the thermodynamic stability of the resulting structures can account for the activation mechanisms experimentally proposed.[38–40] Taking the most stable O vacancy site obtained, the formation energies of the Li-O vacancy pairs have also been calculated, since the coexistence of both vacancies may be favourable in order to maintain the charge neutrality of the crystal. There is one inequivalent oxygen site for $LiMnO_2$, as shown in Fig. 2. For the Li_2MnO_3 crystal and, due to the presence of mixed Li-Mn layers, there are in principle three inequivalent O sites (marked from 1 to 3 in Fig. 2), but the symmetry of the crystal and the similarity of the distance between O and Li ions when the Li is in a pure Li or in a mixed Li-Mn layer (2.12 and 2.08 Å, respectively) reduce the inequivlaent positions to two different formation energies. The difference between them is 0.025 eV/f.u., with the position 1 as the most stable site for O vacancy formation. The effective charges of the Mn ions closer to the O vacancies are 5.53 and 5.16e$^-$ for $LiMnO_2$ and Li_2MnO_3 crystals, respectively, reflecting a small charge transfer from the O^{2-} vacancy site to the neighboring Mn^{3+} (in $LiMnO_2$) or Mn^{4+} (in Li_2MnO_3) ions.
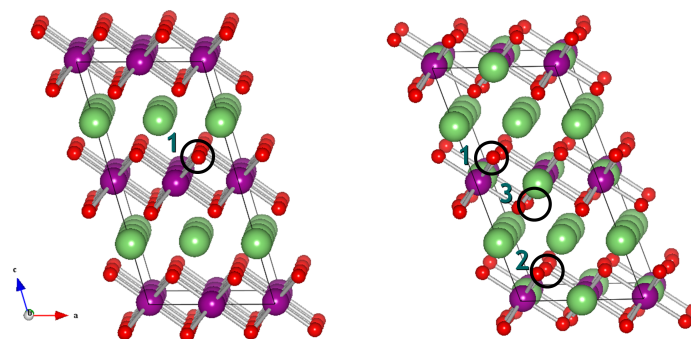
Fig. 2 $LiMnO_2$ (left panel) and Li_2MnO_3 (right panel) with the O vacancy sites considered.

In addition to the O vacancies, we also considered the formation of a Li vacancy, to study the activation mechanism formed by the O-Li vacancy pair. Figure 3 shows the three

different Li vacancy positions considered when the O vacancy is in the most stable position for both $LiMnO_2$ and Li_2MnO_3 crystals. As expected, the most stable locations for Li vacancies are the closest sites to the already existing O vacancy, in order to minimize the Coulomb interaction energy, because of the highly ionic character of the Li-O bond. Both Li vacancy positions are marked as position 1 in Fig. 3 for $LiMnO_2$ and Li_2MnO_3 crystals, respectively. The difference in formation energies between the three different Li vacancy sites is really small, though: 0.044 eV/f.u. for $LiMnO_2$ and 0.057 eV/f.u. for Li_2MnO_3. The formation of Li or O vacancies alone seems to be a very unlikely activation mechanism, since the experimental results report that the oxygen evolution (*i.e.*, removal of excess O, either during the synthesis process or the first cycle of charge/discharge) is the main activation mechanism of the electrochemical activity of Li_2MnO_3 cathode material.[38–40,56] The formation of Li vacancies during the synthesis should entail the loss of Li_2O, something not consistent with the experimental findings.
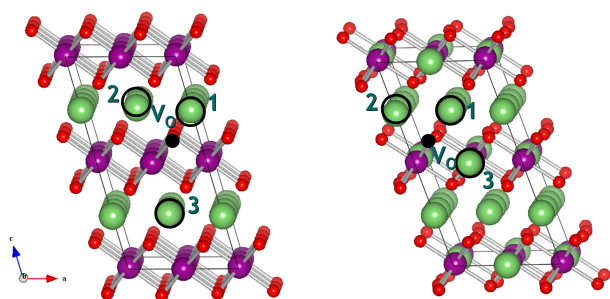
Fig. 3 $LiMnO_2$ (left panel) and Li_2MnO_3 (right panel) with the Li vacancy sites considered, when there is already an O vacancy in its lowest energy configuration.

Given that both O and O-Li pair vacancies are stable and can coexist, we now turn into the required temperature for their formation. Following Ref. [64] and neglecting P and V effects on solids,[55,63,64] the oxygen vacancy formation reaction can be expressed in the following way for $LiMnO_2$ crystal (and in the same manner for Li_2MnO_3):

$$Li_{12}Mn_{12}O_{24} \rightarrow Li_{12}Mn_{12}O_{23} + \frac{1}{2}O_2(g) \qquad (8)$$
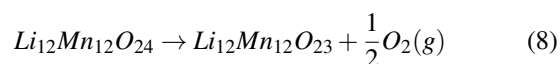
$$\Delta G^0 = G^0(Li_{12}Mn_{12}O_{23}) + \frac{1}{2}G^0(O_2) - G^0(Li_{12}Mn_{12}O_{24})$$
$$\approx E^0(Li_{12}Mn_{12}O_{23}) + \frac{1}{2}H^0(O_2) - T_f S^0(O_2)$$
$$- E^0(Li_{12}Mn_{12}O_{24}), \quad (9)$$

$$T_f = (2E^0(Li_{12}Mn_{12}O_{23}) - E^0(Li_{12}Mn_{12}O_{24})$$
$$+ H^0(O_2))/(S^0(O_2)); \quad (10)$$

and for the Li-O vacancy pair formation reaction:

$$Li_{12}Mn_{12}O_{24} \rightarrow Li_{11}Mn_{12}O_{23} + \frac{1}{2}Li_2O + \frac{1}{4}O_2(g) \qquad (11)$$
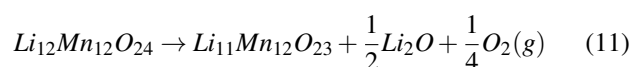
$$\Delta G^0 = G^0(Li_{11}Mn_{12}O_{23}) + \frac{1}{2}G^0(Li_2O) + \frac{1}{4}G^0(O_2)$$
$$- G^0(Li_{12}Mn_{12}O_{24}) \approx E^0(Li_{11}Mn_{12}O_{23}) + \frac{1}{2}E^0(Li_2O)$$
$$+ \frac{1}{4}H^0(O_2) - T_f S^0(O_2) - E^0(Li_{12}Mn_{12}O_{24}), \quad (12)$$

$$T_f = (4E^0(Li_{11}Mn_{12}O_{23}) - E^0(Li_{12}Mn_{12}O_{24})$$
$$+ 2E^0(Li_2O) + H^0(O_2))/(S^0(O_2)). \quad (13)$$

The O vacancy formation temperatures for $LiMnO_2$ and Li_2MnO_3 crystals are, respectively, $\sim$1900 and $\sim$2200 K; higher than for $LiNiO_2$ ($\sim$1100 K) but much lower than for $LiCoO_2$ ($\sim$3500 K).[64] This fact indicates that relatively high temperatures are needed for the formation of O vacancies in both crystals, and that such high formation temperature would ultimately suppress the oxygen evolution and the transformation of Li_2MnO_3 into $LiMnO_2$ during the synthesis. The temperatures for Li-O vacancy pair formation are even higher, $\sim$3000 and $\sim$5000 K, respectively, for $LiMnO_2$ and Li_2MnO_3. Of course these calculated temperatures do not correspond to the exact vacancy formation temperatures since the thermodynamic stability of a particular phase with vacancies must be compared with other phases with vacancies. What our results really imply is that, while relatively medium temperatures can facilitate the oxygen evolution, the Li-O vacancy pair formation is a very unlikely process. This finding confirms the relatively high stability of these two phases and explains why the Li loss (during the charging process) causes a gradual phase transition of the OLO Li_2MnO_3 into the layered $LiMnO_2$. These findings support the experimental evidence of small amount of oxygen deficiencies reported during

Li$_2$MnO$_3$ synthesis[41] or the difficulties to remove Li ions after oxygen loss while keeping the capacity at reasonable operational levels.[35,36]

To confirm the non thermodynamic stability of the O and Li-O pair vacancies, we performed a more systematic investigation of the phase diagram of Li-Mn-O system and its evolution with the temperature. Previous work[55] on the same system was focused on the thermal stability of the spinel phase, whereas in our study we are interested in the relative stability of the Li$_2$MnO$_3$ and LiMnO$_2$ phases. Figure 4 shows the phase diagram at room temperature (RT) of the Li-Mn-O system obtained from our calculations. We assume an oxygen partial pressure of 0.02 MPa (corresponding to ambient conditions). Together with all the reported compounds of the Li-Mn-O system (see Table 1), we also included LiMnO$_2$ and Li$_2$MnO$_3$ with O, Li and Li-O pair vacancies as independent phases of the calculation (Table S1 of the Supplementary Information shows all the obtained formation energies†). At any point different than the nodes, the equilibrium phases are given by the vertices of the triangle bounding every particular composition. The effects of the P, V and entropy terms in solids were again omitted because they are negligible in solids compared to other factors. When calculating the ternary phase diagram at different temperatures (Fig. S1 of the Supplementary Information†), all the finite temperature and entropy effects are taking into account through the oxygen partial pressure (*via* the oxygen chemical potential) with data obtained from the JANAF thermochemical tables,[75] as stated previously. The thermodynamically stable phases are LiMnO$_2$ and Li$_2$MnO$_3$, the cubic spinel LiMn$_2$O$_4$ and the triclinic Li$_2$Mn$_3$O$_7$, Li oxides (Li$_2$O and Li$_2$O$_2$), together with the most stable Mn oxides (MnO, tetragonal spinel Mn$_3$O$_4$ and α−Mn$_2$O$_3$), as it has already been reported.[55] Points 1 and 2 in Fig. 4 denote the positions of the O vacancies for LiMnO$_2$ and Li$_2$MnO$_3$, respectively. None of them (nor the Li-O vacancy pair) are thermodynamically stable at RT. When the temperature is increased up to 800 K (Fig. S1 of the Supplementary Information†), the spinel LiMn$_2$O$_4$ decomposes into the layered LiMnO$_2$, tetragonal Mn$_3$O$_4$ and O$_2$, because the OLO Li$_2$MnO$_3$ has a very narrow range of stability, as we showed in the previous section. Further increase of the temperature up to 1300 K does not modify the phase diagram. Above 2000 K, when the O vacancies can be formed, the Li-Mn-O compounds are no longer thermodynamically stable and they decompose into the corresponding oxides (Li$_2$O and MnO) and O$_2$.

3.3 Solid-state transformation from the layered oxide to the spinel phase

The phase diagrams plotted in Figs. 4 and S1 show that the spinel phase is not thermodynamically stable at the temper-
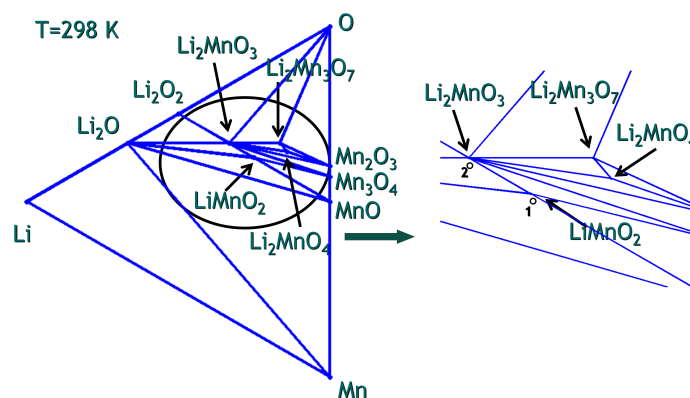
Fig. 4 Calculated ternary phase diagram for the Li-Mn-O system at room temperature. Points 1 and 2 show the position of the Li-O vacancy pair for LiMnO$_2$ and Li$_2$MnO$_3$, respectively (see text for details).

atures at which most of the synthesis procedures are carried out. However, Fig. 4 shows that, at RT, and if Li ions are extracted from the layered oxide phase, the stability domain moves to the right-hand side of the phase diagram (along the Li-Mn composition line) and the spinel structure can be formed. At that point, the equilibrium phases would be the spinel LiMn$_2$O$_4$, the OLO Li$_2$Mn$_2$O$_3$ and the Mn$_2$O$_3$ oxide. During the subsequent cycles, the OLO phase would evolve again into the layered LiMnO$_2$ (the other two stable phases would be now the lithium and manganese oxides Li$_2$O and MnO) but the difference is that, as long as we increase the number of cycles, more amount of the spinel phase will be formed and not decomposed with further Li extraction and/or insertion.

Figure 5 shows a comparison between the formation energies per formula unit of the layered Mn oxide and the spinel phase, with respect to the Li concentration of the host structure. Our results show that, when half of the Li ions are extracted from the host structure during the charging process (*i.e.*, when the stoichiometries of the two phases are the same), the spinel phase formation energy is lower than that of the layered oxide structure. This means that there has to be a thermodynamic driving force facilitating such phase transformation. In an attempt to find the comprehensive kinetic mechanism behind that transformation between the two phases, we performed Solid-State NEB (SS-NEB) calculations,[58] starting with a Mn layered oxide compound, from which half of the Li ions has been extracted, and the spinel phase as the final state. During the SS-NEB minimization, both atomic and cell

degrees of freedom are optimized, in order to find the MEP connecting from initial to final configurations. Figure 6 shows the energy profile obtained in our calculations, together with some of the configurations corresponding to the different intermediate transition states. The spinel phase has a pure Mn layer (purple atoms of Fig. 6) and a mixed Li (green atoms in Fig. 6)-Mn layer, whereas the layered oxide has only pure Li and Mn layers. As Li ions are extracted from the host structure during cycling, the Mn ions can migrate into the (now empty) Li layer. Then, the driving mechanism for the phase transformation is the reduction of the stress between the different layers by "creating" an additional layer within the unit cell to accommodate the new cationic distribution. The rapid nature of this transformation has been attributed to the ease by which Mn^{3+} disproportionates (transforms into a mixture of Mn^{2+} and Mn^{4+}) and moves through the tetrahedral sites of the layered $LiMnO_2$.[55] To visualize the disproportionation of the Mn ions, Fig. S2 of the Supplementary Information† shows a comparison between the initial $Li_{0.5}MnO_2$ layered oxide with all the Mn ions in octahedral sites and the first transition state where some of the Mn ions are already moving through the tetrahedral sites aforementioned. Our Bader charge analysis[79] shows that all the Mn ions in the initial $Li_{0.5}MnO_2$ layered oxide structure are in two different charge states (4.90 or $5.07e^-$, depending on whether the adjacent Li site is occupied or not), whereas all the Mn ions in the transition state are in a larger charge state (between 5.12 and $5.52e^-$). Our results also show (in Fig. 6) that this migration (and the subsequent formation of the new Li-Mn layer) is accompanied by a concomitant reduction of the interlayer stress while the new Li-Mn mixed layer is being "created". The transition states of the insets of Fig. 6 also show that the change is an atom-dominated process (rather than a cell-dominated mechanism), despite of the fact that the two unit cells are remarkably different. The dynamics of the cell shape change is especially predominant after the saddle point has been reached, in order to fit the new shape of the spinel unit cell. The barrier obtained in our calculations is relatively high, 0.94 eV, much larger than that obtained for single atom or cell-dominated processes of phase transformations between more similar phases.[78] As it can be noted in Fig. 6, there is a simultaneous migration of the Li and Mn ions in order to conform the structure of the new spinel phase. Consequently, the SS transformation is not the result of a single migration process (for instance, diffusion of the Mn^{3+} ions through the tetrahedral sites of $LiMnO_2$) and different and simultaneous mechanisms with their respective migration barriers (migration of Li and Mn ions, Coulombic repulsion with the displaced O ions, etc.) should be taken into account in the analysis of the phase transformation. Specifically, the key activation step for this SS transformation are identified as the distortion of the oxygen sub-lattice with the extraction and insertion of Li ions (during cycling), which facilitates the mi-

gration of the Mn^{3+} ions, the formation of Mn-Li anti-site defects, the migration of the Li ions into the tetrahedral sites and, finally, the change in the cell-shape to fit the new Li-Mn mixed layer, once the formation energy of the spinel phase is lower than that of the layered oxide. Recent experimental work[80,81] has confirmed that the transformation of the layered oxide into the new spinel phase can be the result of the diffusion of TM ions from the slab of the layered oxide to the interslab space, to stabilized the delithiated structure. The cracks observed in their diffraction patterns[80] at the edge of the crystal could be the consequence of an increased strain due to Li de-intercalation, accompanied by an in-plane reorganization and the spinel phase formation (see also Figs. 6 and Fig. S2 of the Supplementary Information†). Such spinel phase appears progressively from the shell to the core,[80] which means that the transformation begins at the surface of the cathode material and then it propagates deep into the oxide as long as Li ions are inserted and removed during cycling. Of course, our solid-state mechanism does not correspond exactly to the experimentally observed phase transformation steps, but it provides a comprehensive activation step information, which would be helpful in suppressing the spinel phase transformation by increasing the SS-NEB kinetic barrier (perhaps with appropriate metal doping) and, thus, blocking the layered oxide transformation into the spinel phase.
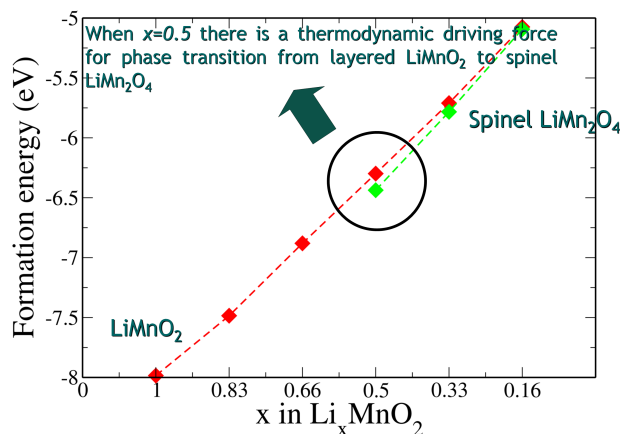
Fig. 5 Formation energy of the layered oxide $LiMnO_2$ and spinel phase $LiMn_2O_4$ as a function of the Li content.

Finally, Fig. 7 shows the same Li-Mn-O phase diagram as shown in Fig. 4, but as a function of the pH. Three particular cases are shown: neutral (pH=7), basic (pH=12) and acidic media (pH=3). In neutral conditions, the OLO Li_2MnO_3 and $LiMnO_2$ layered oxide appear as stable phases, together with the Li oxides and the same Mn oxides that were previously

shown as thermodynamically stable at RT. Under basic conditions, the phase diagram remains practically unchanged, and only the Li peroxide and Mn_2O_3 (Mn^{3+} oxidation state) are decomposed into other reaction products. The phase stabilities are remarkably different in acid conditions, and Fig. 7 shows that both $LiMn_2O_4$ spinel and $Li_2Mn_3O_7$ appear as thermodynamically stable phases. We discussed previously about disproportionation of Mn^{3+} ions as one of the kinetic mechanisms of the transformation of the layered oxide into the spinel phase. It has been recently shown[81] that the formation of Mn^{2+} ions in fragmented pieces of the cathode material with low Li content, due to the continuous extraction of oxygen from the surface structural lattice, which lowers the oxidation valence of Mn for charge neutrality. The particle surface directly contacts the electrolyte and it is easy to be etched by the acidic species coming from the electrolyte, due to its oxidation at high voltages. The attack of those acidic species would accelerate the disproportionation of the Mn^{3+} ions and further reactions involving the decomposition of the spinel phase can also occur. One of them could be the following reaction:[81]

$$2Mn^{3+}(LiMn_2O_4) \rightarrow Mn^{4+}(Li_2Mn_3O_7) + Mn^{2+}(MnO) \quad (14)$$
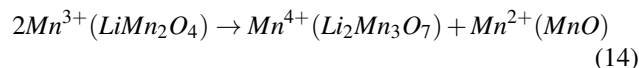
Further degradation of the cathode material and the formation of MnO and Mn^{2+} species results in significantly capacity fading during long-term cycling. In light of this perspective, Fig. 7 and Fig. 1 gain now much more direct relevance to experimental conditions. According to our calculations, the previous reaction has a slight endothermic character (0.6 eV), but it still could be feasible under certain conditions. Indeed, Fig. 1 shows that, under high voltage conditions (more negative $\mu(Li)$), both $LiMn_2O_4$ and $Li_2Mn_3O_7$ appear as stable phases for certain $\mu(O)$ values, which we can easily correlate with acidic conditions, as shown in Fig. 7. Therefore, we can now understand that, in order to prevent the degradation of the cathode material and the observed capacity fading, both phase transformations (from the layered oxide to the spinel and further evolution of the spinel structure under acidic conditions) need to be suppressed.

4 Conclusions

In this work, we have investigated the thermodynamic and electrochemical stability of the different phases of the Li-Mn-O system. Oxygen evolution in the OLO Li_2MnO_3 and Li vacancy formation (probably due to the exchange of proton from nonaqueous electrolyte with the Li^+ ions) have been proposed as the most likely mechanisms for the activation of the electrochemical activity of these cathode materials. Our calculations for the required thermodynamic temperatures of the
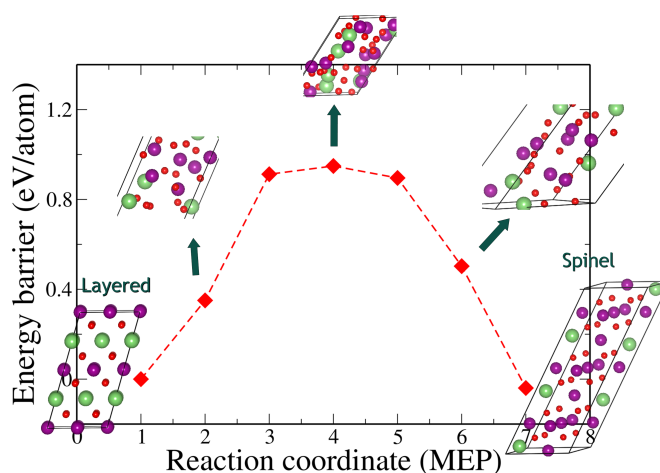
Fig. 6 Solid-State Nudge Elastic Band (SS-NEB) energy barrier for the transformation of the layered oxide $LiMnO_2$ into the spinel phase $LiMn_2O_4$. The inset shows the intermediate images obtained (color code: purple, Mn; green, Li and red, oxygen atoms).

oxygen and Li-O pair vacancy formation show that, although the coexistence of both types of vacancies could increase the stability of the crystal because of the charge neutrality and the strong ionic character of the Li-O bonding, the $LiMnO_2$ and Li_2MnO_3 crystal phases including the vacancies do not appear as stable in the corresponding phase diagrams in both the physical and the chemical potential spaces. Moreover, the high temperatures needed for their formation are incompatible with any practical synthesis temperature, especially for the Li-O vacancy pair formation.

We have also shown that, under acid conditions, both spinel $LiMn_2O_4$ and $Li_2Mn_3O_7$ appear as thermodynamically stable phases, which explains the experimental degradation of the cathode material and the observed capacity fading after long-term cycling.

References

1 M. Armand and J. M. Tarascon, *Nature*, 2008, **451**, 652.
2 A. Prakash, P. Manikandan, K. Ramesha, M. Sathiya, J. M. Tarascon and A. Shukla, *Chem. Mater.*, 2010, **22**, 2857.
3 M. Jiang, B. Key, Y. S. Meng and C. P. Grey, *Chem. Mater.*, 2009, **21**, 2733.
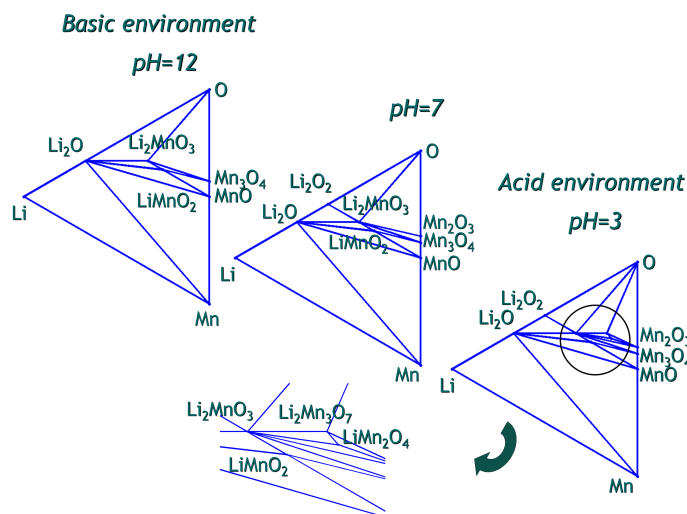
Fig. 7 Calculated ternary phase diagram for the Li-Mn-O system as a function of the pH: neutral (pH=7), basic (pH=12) and acidic (pH=3) environments are shown.

4   C. Kim, M. Noh, M. Choi, J. Cho and B. Park, *Chem. Mater.*, 2005, **17**, 3297.

5   S. KC, K. Xiong, R. C. Longo and K. Cho, *J. Power Sources*, 2013, **244**, 136.

6   K. Mizushima, P. C. Jones, P. J. Wiseman and J. B. Goodenough, *Mater. Res. Bull.*, 1980, **15**, 783.

7   M. Thomas, W. David, J. B. Goodenough and P. Groves, *Mater. Res. Bull.*, 1985, **20**, 1137.

8   J. R. Dahn, U. V. Sacken, M. W. Juzkow and H. Al-Janaby, *J. Electrochem. Soc.*, 1991, **138**, 2207.

9   M. Broussely, F. Perton, J. Labat, R. J. Staniewicz and A. Romero, *J. Power Sources*, 1993, **43**, 209.

10 T. Ohzuku and A. Ueda, *Solid State Ionics*, 1994, **69**, 201.

11 M. Winter, J. Besenhard, M. Spahr and P. Novak, *Adv. Mater.*, 1998, **10**, 725.

12 D. Huang, *Adv. Battery Technol.*, 1998, **11**, 23.

13 H. Yan, X. Huang, L. Zhonghua, H. Huang, R. Xue and L. Chen, *J. Power Sources*, 1997, **68**, 530.

14 Y. Zhou, C. Shen and H. Li, *Solid State Ionics*, 2002, **146**, 81.

15 X. Zhu, Z. Guo, G. Du, P. Zhang and H. Liu, *Surf. Coat. Technol.*, 2010, **204**, 1710.

16 J. Zhao, L. Wang, X. He, C. Wan and C. Jiang, *Int. J. Electrochem. Sci.*, 2010, **5**, 478.

17 H. Zhang, P. J. Baker and P. S. Grant, *J. Am. Ceram. Soc.*, 2010, **93**, 1856.

18 G. Ceder, *Mater. Res. Bull.*, 2010, **35**, 693.

19 P. Kalyani and N. Kalaiselvi, *Sci. Technol. Adv. Mat.*, 2005, **6**, 689.

20 C. Delmas and L. Croguennec, *Mater. Res. Bull.*, 2002, **27**, 608.

21 M. E. Spahr, P. Novák, B. Schnyder, O. Haas and R. Nesper, *J. Electrochem. Soc.*, 1998, **145**, 1113.

22 B. J. Hwang, Y. W. Tsai, R. Santhanam, Y. W. Wu, S. G. Hu, J. F. Lee and D. G. Liu, *J. Power Sources*, 2003, **123**, 206.

23 K. M. Shaju, G. V. S. Rao and B. V. R. Chowdari, *Electrochim. Acta*, 2002, **48**, 145.

24 A. R. Armstrong, N. Dupre, A. J. Paterson, C. P. Grey and P. G. Bruce, *Chem. Mater.*, 2004, **16**, 3106.

25 Z. P. Guo, K. Konstantinov, G. X. Xang, H. K. Liu and S. X. Dou, *J. Power Sources*, 2003, **119-121**, 221.

26 I. Tomeno, Y. Kasuya and Y. Tsunoda, *Phys. Rev. B*, 2001, **64**, 094422.

27 G. Vitins and K. West, *J. Electrochem. Soc.*, 1997, **144**, 2587.

28 Y. I. Jang, B. Huang, Y. M. Chiang and D. R. Sadoway, *Electrochem. Solid-State Lett.*, 1998, **1**, 13.

29 Z. H. Lu and J. R. Dahn, *J. Electrochem. Soc.*, 2002, **149**, A815.

30 M. M.Thackeray, S. H. Kang, C. S. Johnson, J. T. Vaughey, R. Benedek and S. A. Hackney, *J. Mater. Chem.*, 2007, **17**, 3112.

31 C. S. Johnson, N. C. Li, C. Lefief, J. T. Vaughey and M. M.Thackeray, *Chem. Mater.*, 2008, **20**, 6095.

32 Y. Wu, A. V. Murugan and A. Manthiram, *J. Electrochem. Soc.*, 2008, **155**, A635.

33 Z. H. Lu, L. Y. Beaulieu, R. A. Donaberger, C. L. Thomas and J. R. Dahn, *J. Electrochem. Soc.*, 2002, **149**, A778.

34 M. Tabuchi, Y. Nabeshima, T. Takeuchi, K. Tatsumi, J. Imaizumi and Y. Nitta, *J. Power Sources*, 2013, **195**, 834.

35 A. D. Robertson and P. G. Bruce, *Chem. Commun.*, 2002, **23**, 2790.

36 A. D. Robertson and P. G. Bruce, *Chem. Mater.*, 2003, **15**, 1984.

37 Y. Okamoto, *J. Electrochem. Soc.*, 2012, **159**, A152.

38 A. R. Armstrong, M. Holzapfel, P. Novák, C. S. Johnson, S. H. Kang, M. M. Thackeray and P. G. Bruce, *J. Am. Chem. Soc.*, 2006, **128**, 8694.

39 A. Ito, D. Li, Y. Ohsawa and Y. Sato, *J. Power Sources*, 2008, **183**, 344.

40 A. van Bommel, L. J. Krause and J. R. Dahn, *J. Electrochem. Soc.*, 2011, **158**, A731.

41 D. Pasero, V. McLaren, S. de Souza and A. R. West, *Chem. Mater.*, 2005, **17**, 345.

42 J. S. Kim, C. S. Johnson, J. T. Vaughey, M. M. Thackeray, S. A. Hackney, W. S. Yoon and C. P. Grey, *Chem. Mater.*, 2004, **16**, 1996.

43 V. Meunier, J. Kephart, C. Roland and J. Bernholc, *Phys. Rev. Lett.*, 2002, **88**, 75506.

44 J. Reed and G. Ceder, *Electrochem. Solid-State Lett.*, 2002, **5**, A145.

45 G. Ceder, M. K. Aydinol and A. F. Kohan, *Comput. Mater. Science*, 1997, **8**, 161.

46 G. Luo, J. Zhao, X. Ke, P. Zhang, H. Sun and B. Wang, *J. Electrochem. Soc.*, 2012, **159**, A1203.

47 C. Wolverton and A. Zunger, *Phys. Rev. B*, 1998, **57**, 2242.

48 C. Wolverton and A. Zunger, *Phys. Rev. Lett.*, 1998, **81**, 606.

49 Y. Koyama, N. Yabuuchi, I. Tanaka, H. Adachi and T. Ohzuku, *J. Electrochem. Soc.*, 2004, **151**, A1545.

50 K. Kang and G. Ceder, *Phys. Rev. B*, 2006, **74**, 094105.

51 T. Motohashi, T. Ono, Y. Sugimoto, Y. Masubuchi, S. Kikkawa, R. Kanno and M. K. H. Yamauchi, *Phys. Rev. B*, 2009, **80**, 165114.

52 A. van der Ven and G. Ceder, *J. Power Sources*, 2001, **97-98**, 529.

53 K. Kang, Y. S. Meng, J. Bréger, C. P. Grey and G. Ceder, *Science*, 2006, **311**, 977.

54 A. van der Ven and G. Ceder, *Electrochem. Solid-State Lett.*, 2000, **3**, 302.

55 L. Wang, T. Maxisch and G. Ceder, *Chem. Mater.*, 2007, **19**, 543.

56 D. Shin, C. Wolverton, J. R. Croy, M. Balasubramaniam, S. H. Kang, C. M. López-Rivera and M. M. Thackeray, *J. Electrochem. Soc.*, 2012, **159**, A121.

57 Y. Koyama, I. Tanaka, M. Nagao and R. Kanno, *J. Power Sources*, 2009, **189**, 798.

58 D. Sheppard, P. Xiao, W. Chemelewski, D. D. Johnson and G. Henkelman, *J. Chem. Phys.*, 2012, **136**, 074103.

59 G. Kresse and J. Furthmüller, *Comput. Mater. Science*, 1996, **6**, 15.

60 G. Kresse and J. Hafner, *Phys. Rev. B*, 1993, **48**, 13115.

61 P. Blöchl, *Phys. Rev. B*, 1994, **50**, 17953.

62 http://www.fiz-karlsruhe.com/icsd.html.

63 S. P. Ong, L. Wang, B. Kang and G. Ceder, *Chem. Mater.*, 2008, **20**, 1798.

64 Y. Kim, D. Kim and S. Kang, *Chem. Mater.*, 2011, **23**, 5388.

65 C. Barber, D. Dobkin and H. Huhdanpaa, *ACM Trans. Math. Software*,

1996, **22**, 469.

66 P. Thissen, V. Thissen, S. Wippermann, Y. J. Chabal, G. Grundmeier and W. G. Schmidt, *Surf. Sci.*, 2012, **606**, 902.

67 D. Himmel, S. K. Goll, I. Leito and I. Krossing, *Angew. Chem. Int. Ed.*, 2010, **49**, 6885.

68 J. P. Perdew, K. Burke and M. Ernzerhof, *Phys. Rev. Lett.*, 1996, **77**, 3865.

69 H. K. Monkhorst and J. D. Pack, *Phys. Rev. B*, 1976, **13**, 5188.

70 A. Jain, S. P. Ong, G. Hautier, W. Chen, W. D. Richards, S. Dacek, S. Cholia, D. Gunter, D. Skinner, G. Ceder and K. A. Persson, *Appl. Phys. Lett. Mater.*, 2013, **1**, 011002.

71 F. Zhou, M. Cococcioni, C. Marianetti, D. Morgan and G. Ceder, *Phys. Rev. B*, 2004, **70**, 235121.

72 F. Zhou, M. Cococcioni, K. Kang and G. Ceder, *Electrochem. Commun.*, 2004, **6**, 1144.

73 L. Wang, T. Maxisch and G. Ceder, *Phys. Rev. B*, 2006, **73**, 195107.

74 D. Kramer and G. Ceder, *Chem. Mater.*, 2009, **21**, 3799.

75 M. Chase, *JANAF Thermochemical Tables*, American Chemical Society, New York, 1996.

76 H. Jónsson, G. Mills and K. W. Jacobsen, *Classical and Quantum Dynamics in Condensed Phase Simulations*, World Scientific, Singapore, 1998.

77 G. Henkelman, B. P. Uberuaga and H. Jónsson, *J. Chem. Phys.*, 2000, **113**, 9901.

78 G. Henkelman, A. Arnaldsson and H. Jónsson, *J. Chem. Phys.*, 2006, **124**, 044706.

79 W. Tang, E. Sanville and G. Henkelman, *J. Phys.: Condens. Matter*, 2009, **21**, 084204.

80 A. Boulineau, L. Simonin, J. F. Colin, E. Canévet, L. Daniel and S. Patoux, *Chem. Mater.*, 2012, **24**, 3558.

81 J. Zheng, M. Gu, J. Xiao, P. Zuo, C. Wang and J. G. Zhang, *Nano. Lett.*, 2013, **13**, 3824.